THERMODYNAMIC AND FLUIDIC INVESTIGATION OF DIRECT CONTACT SOLID HEAT STORAGE FOR SOLAR TOWER POWER PLANTS

Michael Krüger[1], Joachim Hahn[1] and Stefan Zunft[1]

[1] German Aerospace Center (DLR), Institute of Technical Thermodynamics

Pfaffenwaldring 38-40, 70374 Stuttgart (Germany), Email: michael.krueger@dlr.de

1. Introduction

Central receiver power plants using air as heat transfer medium hold great potential to unite high conversion efficiencies with particularly cost-effective solutions [Romero et al., 2002; Pitz-Paal et al., 2005; Sargent & Lundy, 2003]. Regenerator storage based on directly heated solid media is a suitable heat storage technology for this type of power plants. The technology combines a simple setup with the applicability to highest temperatures and has best prospects for a deployment in large installations [Haeger et al., 1994; Fricker, 2004; Zunft et al., 2009; Gil et al., 2010; Medrano et al., 2010]. These aspects indicate good opportunities for a near-term commercialization [Zunft et al., 2011].

However, this storage type still needs a solar-specific adaptation to be market-ready, where upscalability of today's solutions and cost-efficiency of their implementations are some of the major topics. Among other technical uncertainties, open questions exist with respect to possible air flow maldistributions that may imply the risk of performance losses.

The solar tower Jülich is an experimental central receiver plant, inaugurated in 2009 to serve the needs of further development of the technology [Hennecke, K., et al., 2008; Koll, G., et al., 2009; Pomp, 2010]. The plant uses an open volumetric receiver, a technology developed at DLR. In its primary cycle, air at atmospheric pressure is heated up to temperatures of about 700 °C. This solar heat is transferred to the secondary cycle, a water-steam cycle with 100 bars and 500 °C, driving a 1.5 MWel turbine-generator set.

The plant also integrates a heat storage subsystem, an air-cooled regenerator storage, connected in parallel to the steam generator, see Fig. 1. This storage system has been investigated and its performance has been assessed using measured data obtained from a test campaign performed in March 2010. These results are described in a previous paper [Zunft et al., 2011]. Its storage design and part of these measurements have been used in the following as a data basis.

The objective of the present work was, based on a CFD model of the Jülich tower's storage, to simulate the process of charge and discharge in full load and part load operation, aiming to assess its proneness to maldistributed air flow.

Fig. 1: Jülich solar central receiver plant (left) and plant layout (right)

2. Storage technology and design

One of the key advantages of solar tower power plants and CSP in general is its ability provide demand-oriented electricity generation, supporting a grid-conformant integration of renewable energy. This is achieved with the help of heat storage technologies providing high-temperature heat at 600 °C up to 1000 °C to the power cycle after sunset.

In combination with air-cooled receivers, regenerator-type storage is particularly well suited. With this storage type, a gaseous heat transfer fluid, such as flue gas or air, is in direct contact with a solid storage medium and exchanges heat as it flows along a flow-path through the storage medium.

Regenerator-type storage is used in several high temperature industrial applications. Examples are hot blast stoves, or "Cowper" stoves, in the steel industry, regenerator chambers in the glass industry and regenerative thermal oxidiser (RTO) in industrial air purification systems. Predominantly, alumina-silica, basic and fine ceramic products in form of checker bricks or honeycomb bricks, as well as in form of saddles and spheres for small devices, are used as inventory materials. These existing implementations have been developed for the specific needs of each single target process. Though solar applications of this storage have been looked at in the early 1990ies, its status is still at an early stage.

The Jülich tower plant's storage is one of the rare solar operated implementations of this storage technology. In this system, it is integrated into the tower. It extends over two storeys, close to the location of receiver and steam generator. At rated operation conditions, the storage system is cycled between 120 and 680 ºC and supplies a storage capacity of almost 9 MWh. Further technical specifications are summarised in Tab. 1 below.

Tab. 1: Storage design specifications [Zunft et al., 2011]

Inlet temperature (Charge / Discharge)	680 °C / 120 °C
Outlet temperature (Charge / Discharge)	120-150 °C / 680-640 °C
Charge mass flow	9.4 kg/s
Discharge heat rate	5.7 MWth
Full load discharge period	1.5 h
Pressure loss	< 1500 Pa

The storage consists of four chambers of identical size, connected in parallel in a common tank. The inventory is a stacked arrangement of honeycomb bricks made of fine ceramics material, see Tab. 2 below. The total volume of the inventory amounts to 120 m^3. The storage housing is rectangular in 7 m x 7 m x 6 m size and is made of mild steal, see Fig. 2. An inner insulation made of 0.25 m thick ceramic fibre blankets keeps the surface temperature of the containment below 60 ºC.

During charge operation the hot air from the receiver is divided in two pipes before entering the storage's dome and flows downwards through the storage chambers, forming a moving temperature profile as typically found in regenerators. At the bottom of the housing there are four outlets with one valve each; the junction of the four pipes is located beneath the containment. Reversing the flow direction through the storage starts discharge operation and supplies heat from the storage to the air loop of the steam generator. Details of the storage subsystem are described elsewhere [Zunft et al., 2011].

Tab. 2: Inventory [Zunft et al., 2011]

Honeycombs	60 x 60 cells
Brick dimensions	150x150x150 (mm)
Material	alumina porcelain (C130)
Bulk density	2700 kg/m^3
Specific heat capacity	0.88 kJ/(kg K)
Thermal conductivity	2.1 W/(m K)
Heating surface	1180 m^2/m^3
Free cross section	69 %

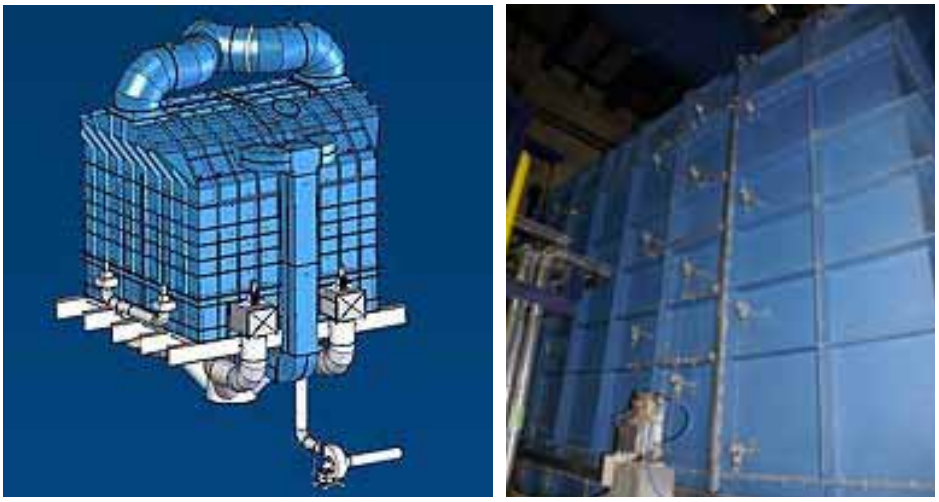

Fig. 2: Storage subsystem: CAD illustration (left) [Zunft et al., 2011] and side view (right)

3. Modeling approach and simulation studies

A CFD model has been set up to describe flow and temperature field in the storage subsystem.

The CFD code solves the incompressible continuity, momentum and energy conservation equations. These again are coupled to the two conservation equations for turbulent kinetic energy and the specific dissipation rate, arising from the k-epsilon approach with standard wall functions used to model the turbulence.

The heat storage inventory itself was modelled as a homogeneous porous medium, a well founded assumption in particular for the case of ceramic honeycombs with large specific heat transfer surfaces. The porous medium's transients enter into the momentum equations through its source terms. The momentum source term S_i *(i=x,y,z)* consists of two parts, the viscous and the inertial loss term.

$$\frac{\partial}{\partial t}\left(\rho_f \vec{v}\right)+\nabla\left(\rho_f \vec{v}\vec{v}\right)=-\nabla p+\nabla\left(\bar{\bar{\tau}}\right)+\rho_f \vec{g}+\vec{S} \quad \text{with:} \qquad \text{(eq. 1)}$$

$$S_i=-\left(\sum_{i=1}^{3}\frac{\mu}{\alpha_i}\cdot v_i+\sum_{i=1}^{3}C_i\cdot\frac{\rho_f}{2}\cdot v_{mag}\cdot v_i\right) \qquad \bar{\bar{\tau}}=\mu\left[\left(\nabla\vec{v}+\nabla\vec{v}^T\right)-\frac{2}{3}\nabla\vec{v}I\right] \qquad \text{(eq. 2)}$$

μ = dynamic fluid viscosity, α = permeability, ρ = fluid density, C = inertial resistance factor, v = superficial velocity component.

Neglecting convective acceleration and diffusion the momentum equation in the porous model simplifies to equation 3, where the resistance coefficients have been obtained from the relevant pressure drop correlations.

$$\frac{dp}{dx_i} = -\left(\frac{\mu}{\alpha_i} \cdot v_i + C_i \cdot \frac{\rho}{2} \cdot v_{mag} \cdot v_i \right) \qquad \text{(eq. 3)}$$

The inventory's flow passage, consisting of 2 mm wide quadratic channels, enforces a laminar flow along through the material with low Reynolds number ranging from 20 to 50. As an implication, the inertial resistance factor in equation 3 can be neglected. An adequate pressure drop correlation is therefore equation 4 [Tiedt 1966].

$$\frac{dp}{dx} = -\frac{0.89 \cdot 32 \cdot \mu}{d_{channel}^2} \cdot v_x \qquad \text{(eq. 4)}$$

where v_x is the physical velocity, which has to be replaced by superficial velocity/ε. This results in the following expression for the permeability:

$$\alpha_i = \left(\frac{0.89 \cdot 32}{\varepsilon \cdot d_{channel}^2} \right)^{-1} \qquad \text{(eq. 5)}$$

For a proper representation of the inventory's channel structure the porous media needs to be modelled as anisotropic: Permeability in the channels axes is calculated as indicated by equation 5 and is set to low values for all other spatial directions.

The porous medium's transients are also implemented in the energy conservation equation. The time derivative of total energy consists of two summands for solid and fluid, weighted with the porosity. The convective term is not affected by the solid because it has no velocity. An effective thermal conductivity is implemented as part of the diffusive term.

$$\frac{\partial}{\partial t}\left(\varepsilon\rho_f E_f + (1-\varepsilon)\rho_s E_s\right) + \nabla\left(\vec{v}\left(\rho_f E_f + p\right)\right) = \nabla\left[k_{eff}\nabla T - \left(\sum_i h_i J_i \right) + \left(\bar{\bar{\tau}}\vec{v}\right) \right] + S_f^h \qquad \text{(eq. 6)}$$

E_f = total fluid energy, E_s = total solid energy, S^h_f = fluid enthalpy source term, ε = porosity
k_{eff} = effective thermal conductivity of the medium

$$k_{eff} = \varepsilon k_f + (1-\varepsilon)k_s \qquad \text{(eq. 7)}$$

k_s = thermal conductivity solid, k_f = thermal conductivity fluid

The temperature field is coupled to the flow field by the temperature dependent material properties, density ρ and the viscosity μ, see equations 1 and 2. Hence, changes in the temperature field caused by heat losses have an effect to the pressure loss (equation 4), which in turn changes the flow field.

To evaluate the uniformity of flow distribution, the uniformity index γ is used [Tsinoglou et. al. 2004]. The uniformity index quantifies the degree of flow uniformity on different planes A in the storage. It is defined as:

$$\gamma = 1 - \frac{1}{2\bar{v}A}\int_A |\bar{v} - v| dA \qquad \bar{v} = \frac{1}{A}\int_A v dA \qquad \text{(eq. 8)}$$

v = velocity component

A computational grid consisting of 2.4 Mio cells has been set up for one of the four chambers. The boundaries to the other chambers have been modelled as symmetry planes, see Fig. 3. The remaining boundaries are assumed to be insulated; applying a thermal conductivity of 0.1 W/(m K) and an external convective heat transfer coefficient of 5 W/(m² K).

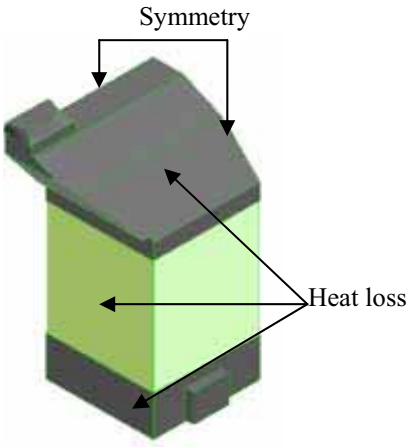

Fig. 3: System boundary of the computational model

To study the temperature field and flow field over a wide range of operation and to evaluate the resulting flow distribution, operational cycles have been calculated in both full and part load. For the part load case, the model parameters are chosen to reproduce test runs of a previously conducted measurement campaign.

The full load case assumes a 100 minutes charge period with a hot air inlet temperature of 680 °C, followed by a 100 minutes discharging period with 120 °C inlet temperature, each with a constant air mass flow of 9.5 kg/s, an initial system temperature of 25 °C and an ambient temperature of 25 °C.

For the part load, the set-point for the mass flow was 2.34 kg/s. The charge temperature starts with 50 °C, increases in a ramp and reaches the target temperature of 625 °C after 120 minutes. After 645 minutes the mass flow decreases to 0.85 kg/s. The discharge period of 428 minutes starts after 708 minutes with mass flow set-point of 2.6 kg/s and a discharge temperature of 90 °C. The initial storage temperature is 8 °C; the ambient temperature is 11 °C.

4. Results

The results for the temperature field shown in the remainder of this work refer to reference planes within the inventory as shown in Fig. 4.

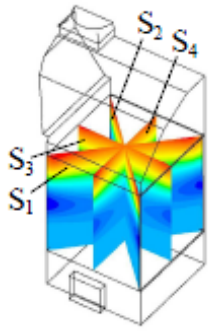

Fig. 4: Reference planes

4.1 Full load

Fig. 5 shows the inventory temperature distribution during the first operating cycle. After the end of charging, the cold end temperature is still at its initial value of 25 °C. The subsequent discharge operation shifts this cold zone through the storage, finally heating it up, see Fig. 5 d-f. After 60 minutes of discharge only a small part of the hot end inventory is in the range of 680 °C. After a further discharge of 40 minutes the storage is nearly completely discharged.

From the temperature profiles a relatively uniform flow distribution can be deduced for both charge and discharge operation. Furthermore, it can be observed that the temperature spread remains smaller in the outer regions, compared to the core zone. At this moment the temperature level in the central upper areas is slightly higher as in the outer regions.

Fig. 6 shows the mass flux distribution on a cross-sectional plane 5 cm below the storage bed entry (hot end). The air mass flow is well distributed during the whole cycle. During the charging the flow is uniformly distributed while during the discharging a decrease in uniformity can be observed. The uniformity index shown in Tab. 3 also confirms this.

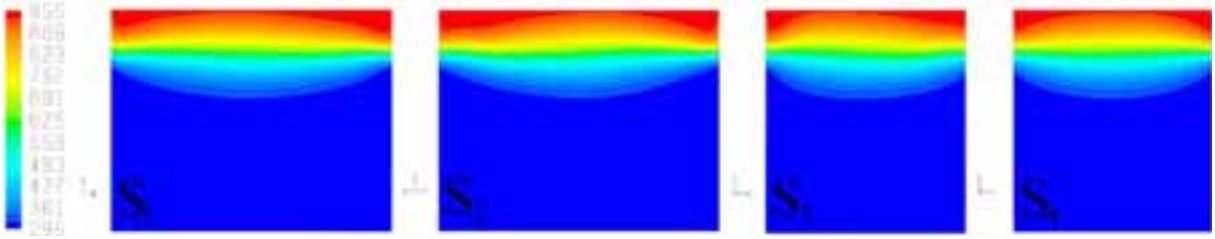

(a) Temperature distribution in Kelvin after 30 min charging

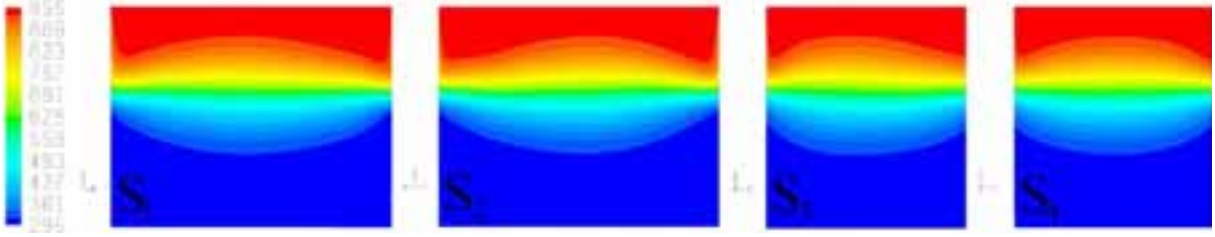

(b) Temperature distribution in Kelvin after 60 min charging

(c) Temperature distribution in Kelvin after 100 min charging

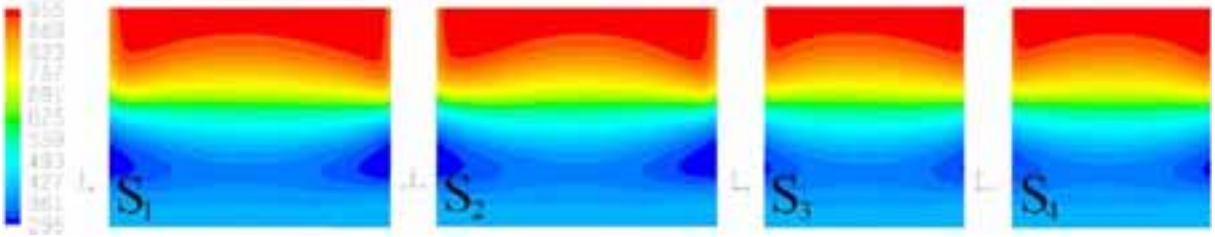

(d) Temperature distribution in Kelvin after 30 min discharging

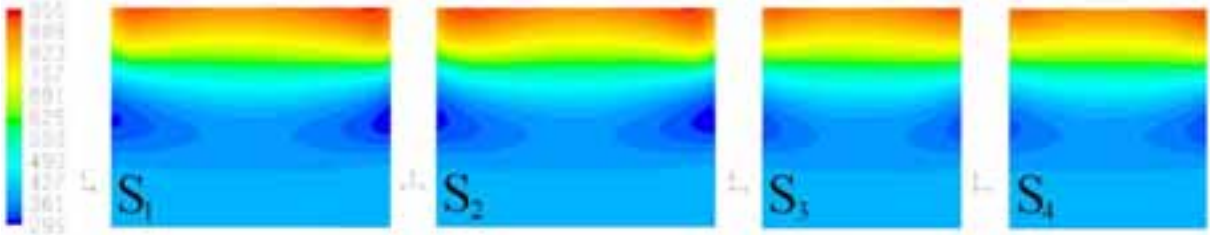

(e) Temperature distribution in Kelvin after 60 min discharging

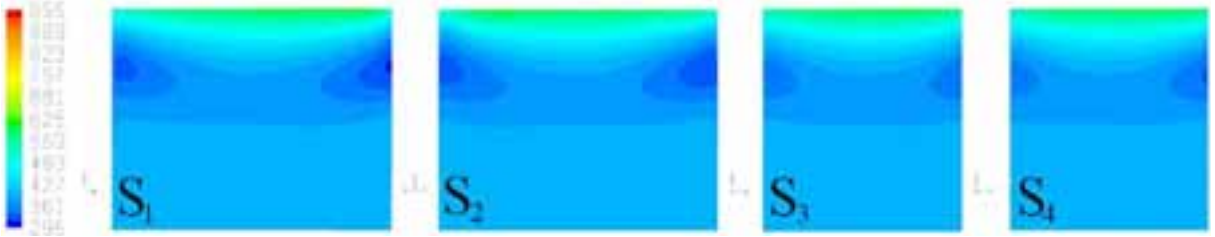

(f) Temperature distribution in Kelvin after 100 min discharging

Fig. 5: Temperature distribution in storage inventory, full load case, vertical cross-sections (according to Fig. 4)

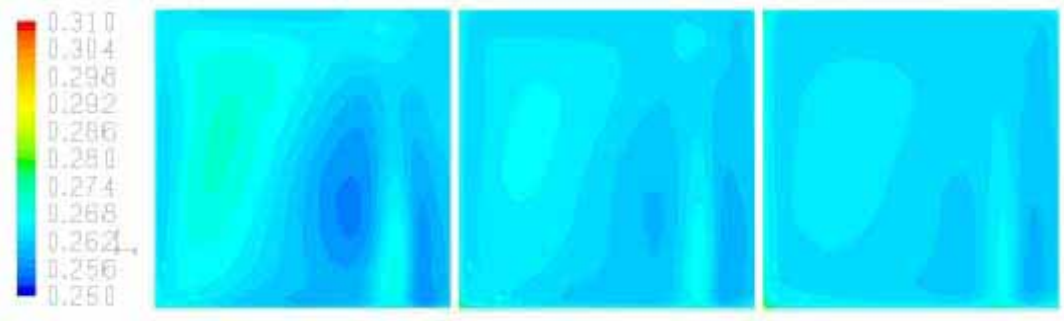

Mass flux in [kg/(s m²)], 5 cm below storage bed entry (hot end), after 30 min, 60 min, 100 min (from left to right) charging

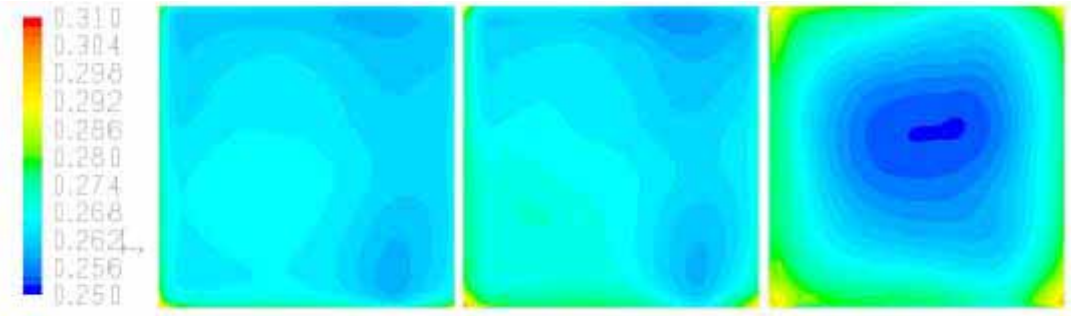

Mass flux in [kg/(s m²)], 5 cm below storage bed entry (hot end), after 30 min, 60 min, 100 min (from left to right) discharging

Fig. 6: Mass flux distribution during charging and discharging, full load case

Tab. 3 Uniformity index, 5 cm below storage bed entry (hot end), full load case

	charging			discharging		
t [min]	30	60	100	30	60	100
γ [-]	0.9943	0.9971	0.9978	0.9964	0.9922	0.9917

Based on the temperature dependence of the air viscosity, a plausibility check of these results becomes possible: An air viscosity rising with increasing temperature induces a higher flow resistance or, vice versa, lower flow resistances in relatively colder areas. If now, due to maldistributions in the dome, zones of locally increased flow velocities exist, these zones experience an increased heating rate and are thus heated up more rapidly during charging. As the increasing flow resistance represents a counteracting, self-regulating effect, the resulting flow tends to improve its uniformity during the charge cycle.

During discharge, in contrary, a locally increased flow induces a more rapid cooling of that zone. This effect is enforced by a decreasing flow resistance – a self-reinforcing mechanism provoking a potential maldistribution during the discharging period.

4.2 Part load

Fig. 7 shows the temperature distribution in the storage inventory during the part load cycle. Again, a satisfying uniformity of flow is visible. Also, as before, the temperature spread is smaller in the outer regions than in the core zone.

Compared to the previous calculation run, the charging period is now long enough heat up all part of the inventory. After 257 minutes of discharge only a small part of the upper inventory shows temperatures in the range of 625 °C. After 430 minutes the discharging is stopped, the storage is not completely discharged. The temperature level in the core's upper areas is slightly higher than in the outer regions. Compared to the full load case the calculated temperature field show a less pronounced symmetry. This is due to an increased

significance of thermal losses resulting from a longer cycle period.

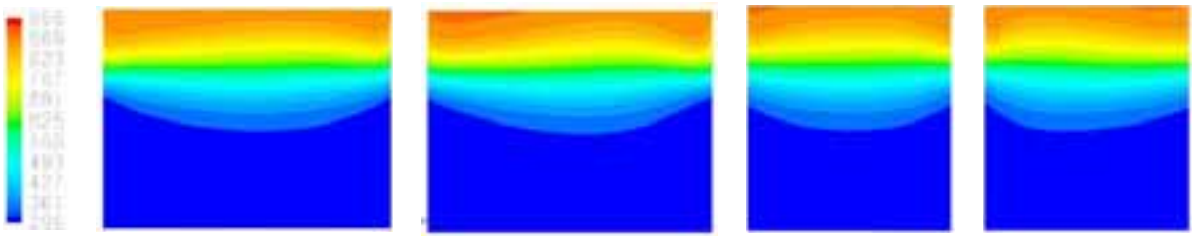

(a) Temperature distribution in Kelvin after 175 min charging

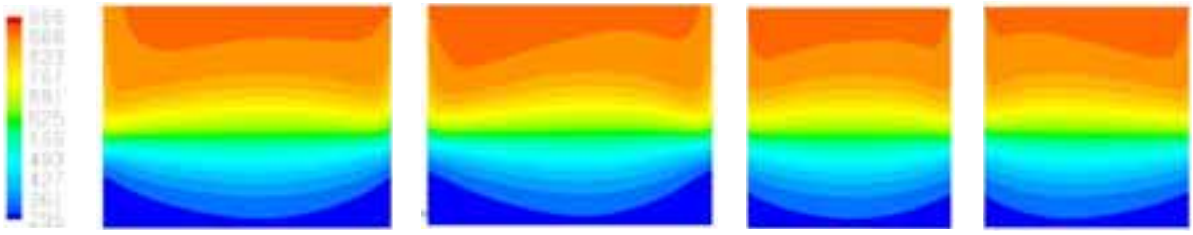

(b) Temperature distribution in Kelvin after 360 min charging

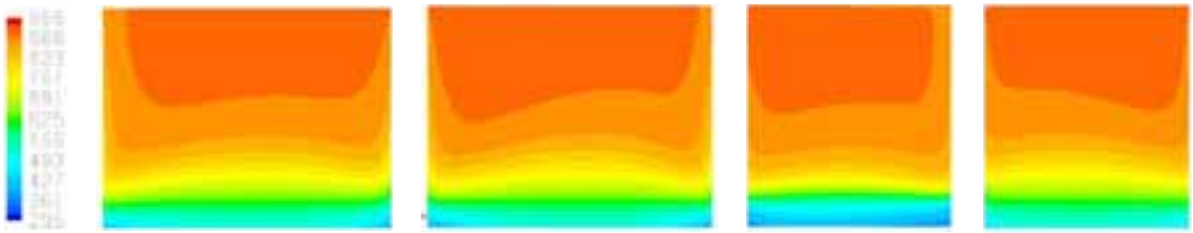

(c) Temperature distribution in Kelvin after 534 min charging

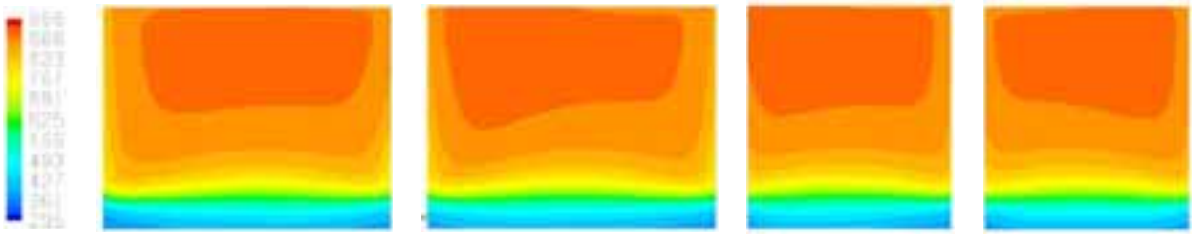

(d) Temperature distribution in Kelvin after 72 min discharging

(e) Temperature distribution in Kelvin after 257 min discharging

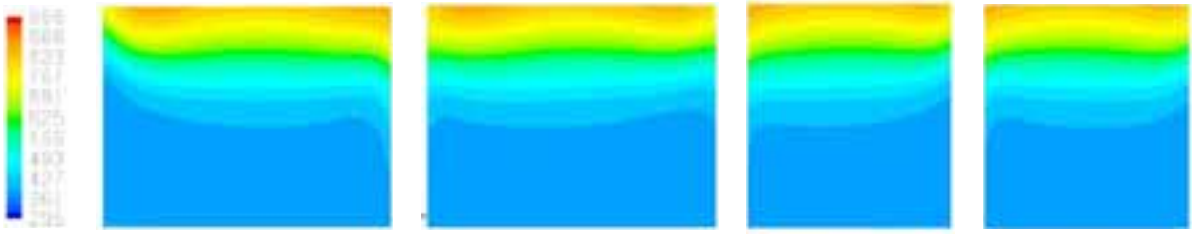

(f) Temperature distribution in Kelvin after 430 min discharging

Fig. 7: Temperature distribution in storage inventory, part load case, vertical cross-sections (according to Fig. 4)

Fig. 8 shows the mass flux distribution on a virtual plane 5 cm below the storage bed entry (hot end). As in the full load case, the air mass flow is well distributed during the whole cycle. During the charging a uniforming of the flow and for discharging a decreasing uniformity can be observed. The corresponding uniformity indexes are given in

Tab. 4.

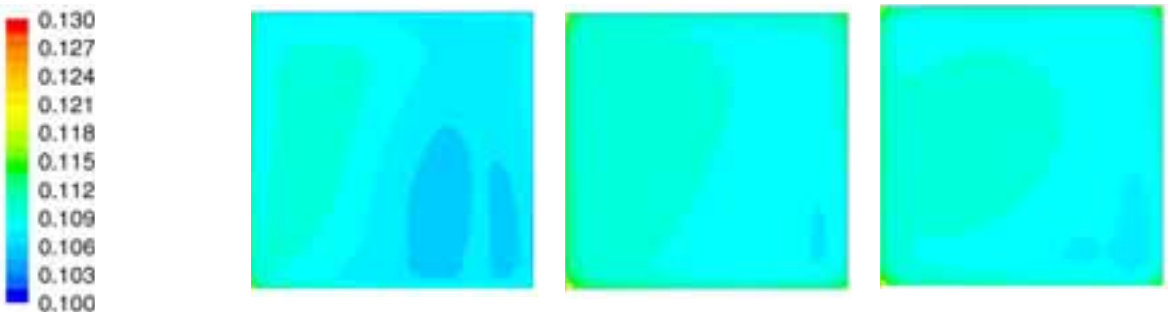

Mass flux in [kg/(s m²)], 5 cm below storage bed entry (hot end), after 175 min, 360 min, 534 min (from left to right) charging

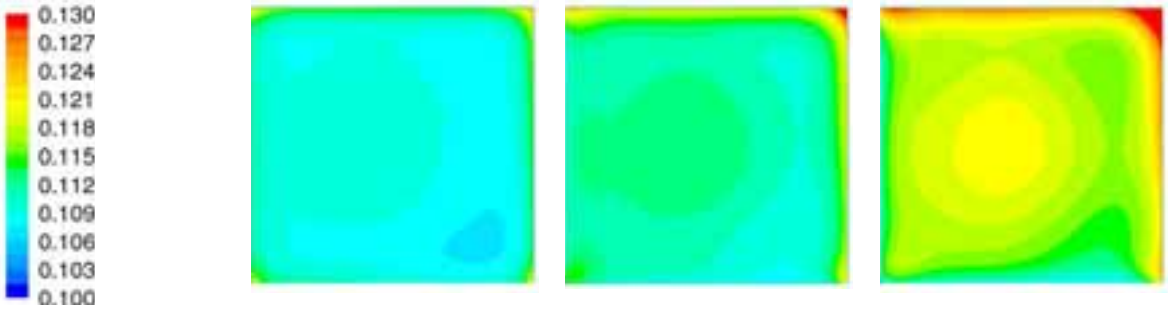

Mass flux in [kg/(s m²)], 5 cm below storage bed entry (hot end), after 72 min, 257 min, 430 min (from left to right) discharging

Fig. 8: Mass flux distribution for charging and discharging, part load case

Tab. 4 Uniformity index, 5 cm below storage bed entry (hot end), part load case

	charging			discharging		
t [min]	175	360	534	72	257	430
γ [-]	0.9961	0.9975	0.9973	0.9971	0.9959	0.9940

5. Summary and conclusions

On the way to cost-efficient market-scale regenerator storage for use of air-cooled receivers, the flow-related design aspects offer room for further cost savings. This includes the quality of flow distribution, a property depending, amongst other, on the volume of the storage's dome.

With this goal in mind, a regenerator-type heat storage forming part of Jülich solar tower plant was modelled by using commercial CFD software. The operation conditions selected for the simulation runs were chosen after the test runs of a measurement campaign. Temperature field and flow field were evaluated for chosen cross sections of the inventory and for chosen time intervals of the cycle.

The results show only small deviations from a uniform flow distribution, becoming apparent in calculated uniformity indexes close to 1. Accordingly, for this specific storage implementation and for the operational conditions under consideration, a temperature-induced maldistribution is not to be expected. It can be concluded that a smaller dome had led to comparable flow quality and that up-scaled version of the storage could benefit from such cost reduction potential.

The underlying mechanism of the flow disturbance is attributed to temperature-related changes of the air viscosity. The simulation results also indicate, that the resulting flow maldistribution have a 'self-healing' effect during the charge period. In contrast, during discharge period a self-reinforcing tendency to a declined flow uniformity occurs and could potentially amplify initially small distribution errors.

These results and the understanding of these phenomena provide valuable hints towards a further improved storage design.

6. References

Dreißigacker, V. et al.: Thermo-mechanical analysis of packed beds for large-scale storage of high temperature heat. Heat Mass Transfer 46 (2010) pp. 1199–1207

Fricker, H. W.: Regenerative thermal storage in atmospheric air system solar power plants. Energy 29 (2004) pp. 871–881

Gil, A. et al.: State of the art on high temperature thermal energy storage for power generation. Part 1 – Concepts, materials and modellization, Renewable and Sustainable Energy Reviews 14 (2010) pp. 31–55

Haeger, M. et al.: Phoebus Technology Program Solar Air Receiver (TSA). "Operational Experiences with the Experimental Set-Up of a 2.5 MWth Volumetric Air Receiver (TSA) at the Plataforma Solar de Almería". PSA-TR02/94, 1994.

Hennecke, K. et al.: Solar power tower Jülich. First test and demonstration plant for open volumetric receiver technology in Germany. 14th SolarPACES Symposium, Las Vegas (NV), March 4-7, 2008

Koll, G. et al.: The solar tower Jülich – a research and demonstration plant for central receiver systems. 15th SolarPACES Symposium, Berlin, Germany, September 15-18, 2009

Medrano, M. et al.: State of the art on high-temperature thermal energy storage for power generation. Part 2 – Case studies, Renewable and Sustainable Energy Reviews 14 (2010) pp. 56–72

Pitz-Paal, R. et al.: European Concentrated Solar Thermal Road-Mapping (ECOSTAR): Roadmap Document. SES-CT-2003-502578, 2005

Pomp, S. et al.: The Solar Tower Jülich – First Operational Experiences and Test Results. 16th SolarPACES Symposium, Perpignan, Frankreich, September 21-24, 2010

Romero, M. et al.: An Update on Solar Central Receiver Systems, Projects, and Technologies. Transactions of the ASME, Journal of Solar Energy Engineering 124 (2002), pp 98-108

Sargent & Lundy: Assessment of Parabolic Trough and Power Tower Solar Technology Cost and Performance Forecasts. NREL/SR-550-34440, 2003

Tiedt, W: Tech. Report No. 4 issued by the Institute for Hydraulics and Hydrology in Tech. Univ. of Darmstadt, March

Tsinoglou, D. N. et al.: Transient modelling of flow distribution in automotive catalytic converters. Applied Mathematical Modelling 28 (2004), pp. 775–794

Zunft, S. et al.: High-temperature heat storage for air-cooled solar central receiver plants: a design study. 15th SolarPACES Symposium, Berlin, Germany, September 15-18, 2009

Zunft et al.: Jülich Solar Power Tower – Experimental Evaluation of the Storage Subsystem and Performance Calculation. Journal of Solar Energy Engineering 133 (2011) pp. 1019-1023